ADVANCED PHYSICS RESEARCH Open Access
www.advphysicsres.com

Pressure-Induced Superconductivity and Structure Phase Transition in SnAs-Based Zintl Compound $SrSn_2As_2$

Weizheng Cao, Juefei Wu, Yongkai Li, Cuiying Pei, Qi Wang, Yi Zhao, Changhua Li, Shihao Zhu, Mingxin Zhang, Lili Zhang, Yulin Chen, Zhiwei Wang, and Yanpeng Qi**

Layered SnAs-based Zintl compounds exhibit a distinctive electronic structure, igniting extensive research efforts in areas of superconductivity, topological insulators, and quantum magnetism. In this paper, the crystal structures and electronic properties of the Zintl compound $SrSn_2As_2$ upon compression are systematically investigated. Pressure-induced superconductivity is observed in $SrSn_2As_2$ with a nonmonotonic evolution of superconducting transition temperature T_c. Theoretical calculations together with high-pressure synchrotron X-ray diffraction and Raman spectroscopy have identified that $SrSn_2As_2$ undergoes a structural transformation from a rhombohedral $R\bar{3}m$ phase to the monoclinic $C2/m$ phase. Beyond 28.3 GPa, T_c is suppressed due to a reduction of the density of state (DOS) at the Fermi level. The discovery of pressure-induced superconductivity, accompanied by structural transitions in $SrSn_2As_2$, greatly expands the physical properties of layered SnAs-based compounds and provides new ground states upon compression.

1. Introduction

Zintl phases, a unique category of intermetallic compounds, were first introduced by E. Zintl in 1939, and have attracted considerable research attention.[1] Zintl compounds are characterized by their intricate chemical bonding and structural features. Their valence bonding modes can encompass ionic, metallic, and covalent interactions, reflecting their remarkable compositional and structural diversity.[2] Zintl compounds are primarily categorized into layered, chain, cage, etc. These classifications often include AB_2X_2, $A_5B_2X_6$, AX_3, and B_4X_3, with A representing alkali, alkaline-earth or rare-earth metals, B representing transition metals, and X representing metalloids.[3] With flexible structures, Zintl compounds possess a broad spectrum of physical properties, encompassing superconductivity, topological properties, magnetic order thermoelectricity, etc.[3i,4]

In recent years, the layered SnAs-based Zintl compounds have attracted much attention.[5] Layered Zintl compound $NaSn_2As_2$ crystallizes in trigonal $R\bar{3}m$ structure, where Na^+ ions are separated by two honeycombs $[SnAs]^{2-}$ layers. The adjacent honeycomb layers interaction is via van der Waals (vdW) forces.[5f,i] At ambient pressure, $NaSn_2As_2$ shows bulk superconductivity with T_c of 1.3 K.[5f,i] It should be noted that $NaSn_2As_2$ is a nonelectron-balanced compound,

---

W. Cao, J. Wu, C. Pei, Q. Wang, Y. Zhao, C. Li, S. Zhu, M. Zhang, Y. Chen, Y. Qi
School of Physical Science and Technology
ShanghaiTech University
Shanghai 201210, China
E-mail: qiyp@shanghaitech.edu.cn

Y. Li, Z. Wang
Centre for Quantum Physics
Key Laboratory of Advanced Optoelectronic Quantum Architecture and Measurement (MOE)
School of Physics
Beijing Institute of Technology
Beijing 100081, China
E-mail: zhiweiwang@bit.edu.cn

The ORCID identification number(s) for the author(s) of this article can be found under https://doi.org/10.1002/apxr.202300149

DOI: 10.1002/apxr.202300149

Y. Li, Z. Wang
Beijing Key Lab of Nanophotonics and Ultrafine Optoelectronic Systems
Beijing Institute of Technology
Beijing 100081, China

Y. Li, Z. Wang
Material Science Center
Yangtze Delta Region Academy of Beijing Institute of Technology
Jiaxing 314011, China

Q. Wang, Y. Chen, Y. Qi
ShanghaiTech Laboratory for Topological Physics
ShanghaiTech University
Shanghai 201210, China

L. Zhang
Shanghai Synchrotron Radiation Facility
Shanghai Advanced Research Institute
Chinese Academy of Sciences
Shanghai 201203, China

Y. Chen
Department of Physics
Clarendon Laboratory
University of Oxford
Parks Road, Oxford OX1 3PU, UK

Y. Qi
Shanghai Key Laboratory of High-resolution Electron Microscopy
ShanghaiTech University
Shanghai 201210, China

containing Sn^{2+} ions with lone pairs of electrons.[5c,6] In contrast to $NaSn_2As_2$, the isostructural compound $EuSn_2As_2$ is electron-balanced one. $EuSn_2As_2$ contains magnetic Eu^{2+} ions, forming a peelable layered magnetic Zintl phase.[7] A transition from the paramagnetic (PM) to the antiferromagnetic (AFM) phase in $EuSn_2As_2$ occurs around T_N–24 K.[7a,8] Below T_N, $EuSn_2As_2$ is ferromagnetic in the *a,b* plane and antiferromagnetic between adjacent layers, forming an A-type AFM. A combination of first-principles calculations and angle-resolved photoemission spectroscopy (ARPES) experiments reveal that $EuSn_2As_2$ is a magnetic topological insulator (TI), characterized by the absence of an observable gap in the Dirac topological surface states (SSs). Besides, $EuSn_2As_2$ transforms from a strong TI with PM state to an axial insulator with AFM state below T_N.[9] T_N shows a linear increase with pressure below 10 GPa, attributed to the enhanced interlayer magnetic exchange coupling among Eu^{2+} ions.[10] Beyond ≈14 GPa, $EuSn_2As_2$ experiences a two-step high-pressure structural transformation, giving rise to a novel monoclinic configuration. The bent Sn—Sn bonds become planar and form honeycomb Sn sheets, coinciding with the emergence of superconductivity ≈4 K.[11]

$SrSn_2As_2$ is the sister compound of $EuSn_2As_2$, which remains relatively less explored. Theoretical calculations propose that $SrSn_2As_2$ is a potential candidate for the novel 3D Dirac semimetal.[12] The ARPES results presented a band reversal feature near the Γ point, indicating that $SrSn_2As_2$ may be a new topological insulator.[13] Given that $EuSn_2As_2$ is superconducting under high pressure, it is interesting to explore novel quantum phenomena in $SrSn_2As_2$ upon compression. Hence, we systematically investigate the structural and electronic properties of the SnAs-based Zintl compound $SrSn_2As_2$ under high pressure. Interestingly, we observe the pressure-induced superconductivity in $SrSn_2As_2$, with a nonmonotonic evolution of T_c. Our theoretical calculations reveal that $SrSn_2As_2$ undergoes a structural transformation from a rhombohedral to a monoclinic phase under high pressure, as evidenced by both X-ray diffraction (XRD) and Raman data. The electronic band structure of the high-pressure phase and the evolution of T_c are also discussed.

2. Results and Discussion

Prior to high-pressure measurements, we first check the sample quality by single-crystal and powder XRD diffractions. The single crystal XRD pattern on the (00l) flat surface of the sample shows sharp diffraction peaks (**Figure** 1a). The inset of Figure 1b shows the chemical compositional analysis results using EDX, illustrating a Sr:Sn:As atomic ratio of 20.45:38.97:40.59, which is consistent with the nominal composition. In addition, we further performed the powder XRD for phase examinations. As shown in Figure 1b, all the Bragg peaks can be indexed into a rhombohedral structure with the space group $R\bar{3}m$. The calculated lattice parameter are $a = 4.2012(7)$ Å and $c = 26.7155(4)$ Å, in agreement with the previous report.[5a] The consistency between powder and single crystal XRD measurements guarantees the correct phase. The ambient crystal structure of $SrSn_2As_2$ is shown in Figure 1c, which is identical to the configuration of $EuSn_2As_2$ and $NaSn_2As_2$.[5i,11a] Then, we performed transport measurements at ambient pressure. Figure 1d shows the resistivity of $SrSn_2As_2$ as a function of temperature, showing typical metallic behavior with residual resistivity ratio (RRR) = 2.31.

Since $NaSn_2As_2$ showed superconductivity at ambient pressure and $EuSn_2As_2$ achieved superconductivity upon compression, it is natural to explore superconductivity in $SrSn_2As_2$ using high-pressure technology. Hence, we investigated the effect of high pressure on $SrSn_2As_2$ single crystals. **Figure** 2a shows the electrical resistivity $\rho(T)$ of $SrSn_2As_2$ at various pressures. Increasing pressure induces a continuous suppression of the overall magnitude of $\rho(T)$, which is typical behavior of metal under high pressure. As shown in Figure 2b, the resistivity of $SrSn_2As_2$ drops abruptly at ≈2.5 K at 10.3 GPa. The resistivity drop becomes more pronounced upon further compressing. Above 28.3 GPa, zero resistivity is observed at low temperatures, indicating a superconducting transition. The superconducting transition temperature T_c (90% drop of the normal state resistivity) reaches 4.63 K at $P = 28.3$ GPa. As plotted in Figure 2c, T_c decreases slowly beyond this pressure, and the superconductivity persists up to 53.5 GPa. The temperature dependence of transition width ΔT_c (10–90% of the normal state resistivity at T_c) is in Figure 6 and Figure S1 (Supporting Information). The transition width ΔT_c has a sharp decline from 2.07 to 0.44 K in the pressure range from 22.9 to 34.4 GPa. ΔT_c reflects the superconducting stated disturbance originating from the thermodynamic fluctuations, the applied magnetic field, the presence of secondary crystalline phases, the applied pressure, etc.,[14] which needs further evidence to confirm its origin. The overall behavior of T_c reveals a nonmonotonic evolution under high pressure. Interestingly, T_c is also observed during decompression, and the superconducting transition persists until recovery to 14.9 GPa.

To gain insight into the superconducting transition, we applied an external magnetic field to samples subjected to 28.3 and 48.1 GPa, respectively. Figure 2d,e demonstrate that the T_c is continuously suppressed with increasing magnetic field and the superconducting transition could not be observed above 1.8 K at ≈2.5 T. This confirms that the sharp drop of $\rho(T)$ ≈4 K in $SrSn_2As_2$ originates from a superconducting transition. The upper critical field $\mu_0 H_{c2}$ is determined from the 90% point on the resistivity transition curve, and the plot of temperature normalized $H_{c2}(T)$ is shown in Figure 2f. By fitting the data using the Ginzburg–Landau (G-L) formula $\mu_0 H_{c2}(T) = \mu_0\ H_{c2}(T)(1-t^2)/(1+t^2)$, where $t = T/T_c$ is the reduced temperature with zero-field superconducting T_c. The extrapolated upper critical fields $\mu_0 H_{c2}$ (0) at 28.3 and 48.1 GPa are 2.05 and 2.41 T, which yields a Ginzburg-Landau coherence length $\xi_{GL}(0)$ of 12.68 and 11.69 nm, respectively.

The transition width ΔT_c drastically changed at ≈30 GPa, and the slopes of $\mathrm{d}H_{c2}/\mathrm{d}T$ are notably different: −0.53 and −0.69 T/K for 28.3 and 48.1 GPa, respectively. Our results suggest that the nature of the superconducting state beyond 30 GPa may differ from that of the initial superconducting one. In order to identify the structural stability of $SrSn_2As_2$ under high pressure, we have performed high-pressure in situ synchrotron XRD and Raman spectroscopy measurements. The XRD patterns of $SrSn_2As_2$ collected at different pressures are shown in **Figure** 3a. As the pressure increases, all diffraction peaks move to higher angles due to lattice contraction, and no structural phase transition is observed at pressures up to 29.8 GPa. Above 33.0 GPa, additional diffraction peaks appear, indicating a structural phase transition.

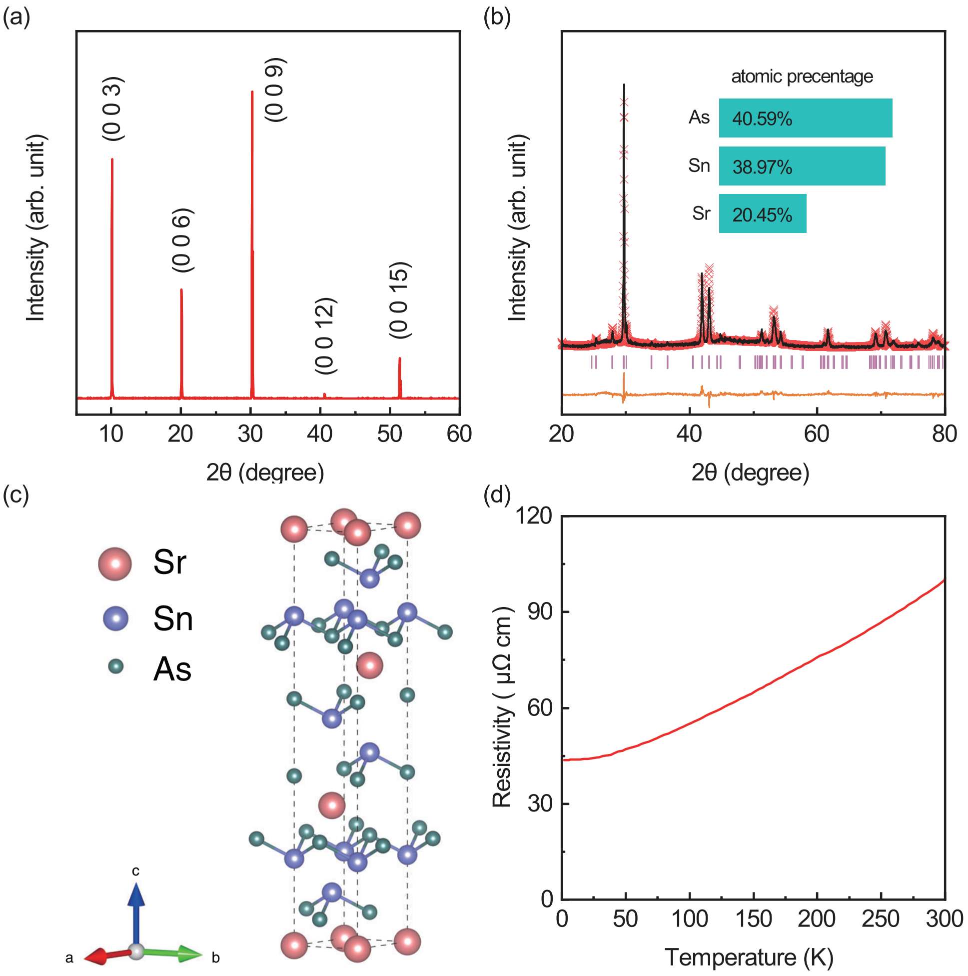

Figure 1. a) The X-ray diffraction peaks from the *ab* plane of $SrSn_2As_2$ single crystal. b) Powder XRD pattern of $SrSn_2As_2$ at room temperature. Inset: the elemental content of $SrSn_2As_2$. c) The crystal structure of $SrSn_2As_2$ with a space group $R\bar{3}m$. Pink, violet, and green balls represent Sr, Sn, and As atoms, respectively. d) Temperature dependence of resistivity for $SrSn_2As_2$ single crystal at ambient pressure.

Figure 3b presents the Raman spectra of $SrSn_2As_2$ under various pressures up to 55.5 GPa. With increasing pressure, the interaction force between adjacent layers increases and all four phonon modes exhibit blue shift, which is analogous to $EuSn_2As_2$.[11b] The Raman signals of the A^2_{1g} mode become significant, while E^2_g mode decreases monotonically. An abrupt disappearance of Raman peaks for pressure beyond 33.6 GPa indicates the structural phase transition to a high-pressure phase. The evolution of the Raman spectra is consistent with our synchrotron XRD patterns and provides further evidence for pressure-induced structural phase transition.

It should be emphasized that by only relying on the experimental data, the structural solution of high-pressure phases is not possible, because the XRD peaks are rather weak and broad. Hence, we performed the structure predictions at 30 and 50 GPa, respectively. In each search, structures were evaluated within 25 generations with 30 structures per generation, and the ambient stable structure $R\bar{3}m$ was treated as a seed structure. We found one stable monoclinic structure with space group $C2/m$ under high pressure, as shown in the inset of **Figure 4a**. The buckled Sn—Sn bonds become planar and form honeycomb-like Sn sheets, meanwhile, the SnAs layers further connect to each other via the As—As bonds across the Sr layers to form zigzag As chains between the Sn sheets. This 3D monoclinic structure comprising honeycomb-like Sn sheets and zigzag As chains resembles the situation in $EuSn_2As_2$ identified under high pressure.[11a] As the enthalpy difference relative to $R\bar{3}m$ structure in Figure 4a, the enthalpy of $C2/m$ structure is below that of $R\bar{3}m$ above 22 GPa, suggesting that $C2/m$ structure is more energetically stable under high pressure. Then we calculated the phonon spectrum of $C2/m$ structure under high pressure, as plotted in Figure 4b,c. There are no imaginary frequencies in the phonon dispersion for $C2/m$ phase above 25 GPa, illustrating its dynamical stability. In summary, our theoretical and experimental results suggest that there is a structural phase transition from $R\bar{3}m$ phase to $C2/m$ phase under high pressure.

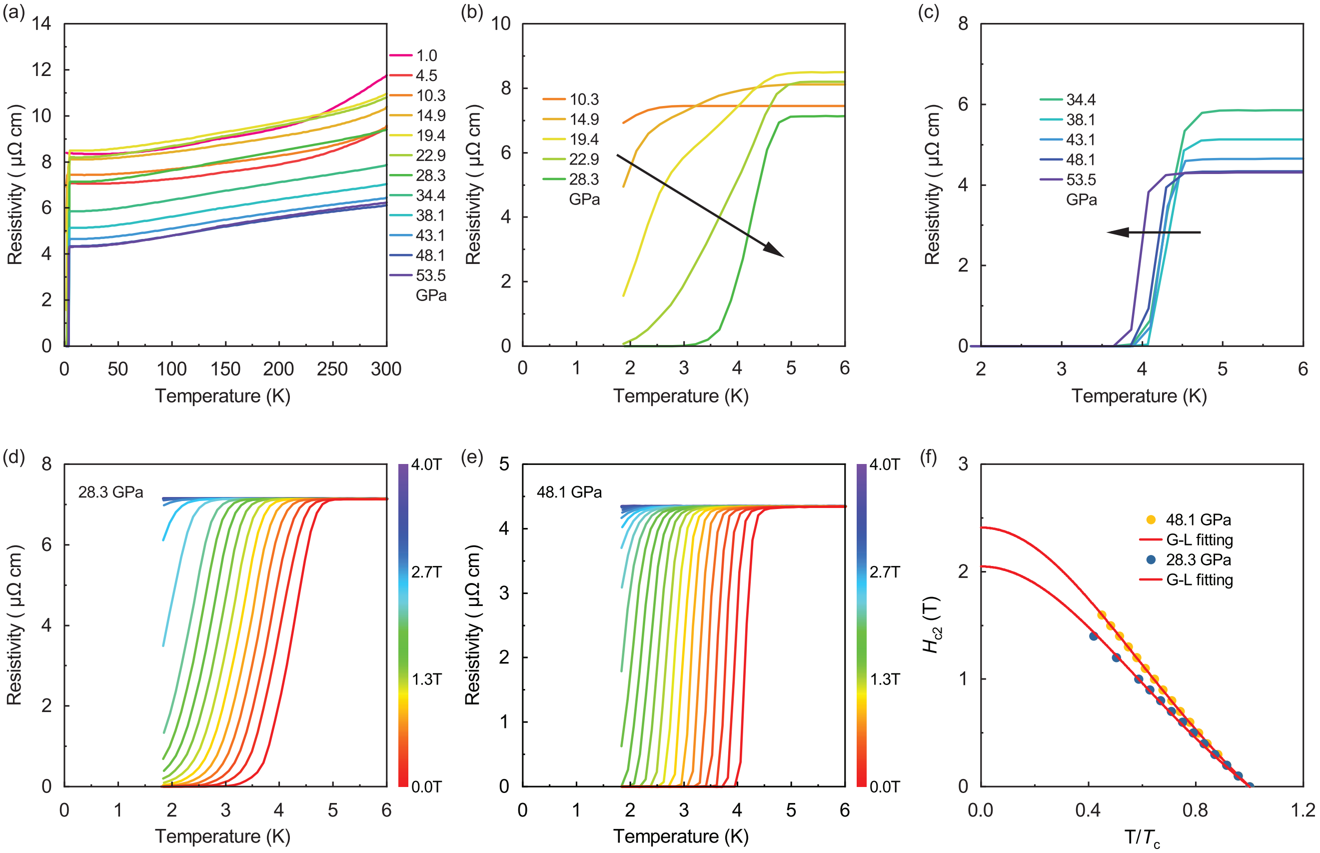

Figure 2. a) Pressure dependence of electrical resistivity of $SrSn_2As_2$ at a temperature range of 1.8–300 K in run II. b,c) Pressure-induced superconductivity. The temperature-dependent resistivity at various pressures from 10.3 to 53.5 GPa in the vicinity of the superconducting transition. d,e) Resistivity of $SrSn_2As_2$ as a function of temperature under different magnetic fields at a pressure of 28.3 and 48.1 GPa, respectively. f) H_{c2} as a function of normalized temperature at the pressure of $SrSn_2As_2$ at 28.3 and 48.1 GPa, respectively. T_c is determined as the 90% drop of the normal state resistivity. The solid lines represent the Ginzburg–Landau (G–L) fitting.

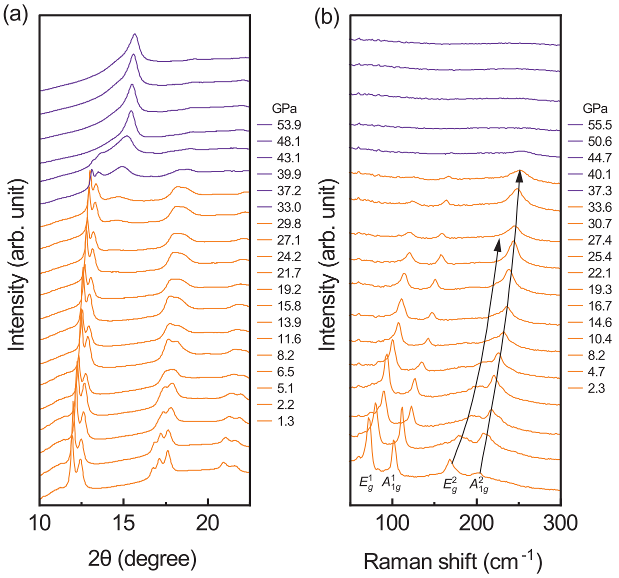

Figure 3. Structure evolution of $SrSn_2As_2$ under high pressure. a) XRD patterns and b) Raman spectra of $SrSn_2As_2$ at various pressures.

Next, we calculated the electronic structures of $C2/m$ structure under high pressure. As depicted in **Figure** 5a,c, the valence bands and conduction bands cross the Fermi energy in the band structures of $C2/m$ phase, exhibiting typical metal characteristics. We can observe steep conduction bands crossing the Fermi energy, which is beneficial for superconductivity. The corresponding partial density of states (PDOS) is shown in Figure 5b,d. The Sn atoms make the main contribution at the Fermi energy, and the total density of states (DOS) at Fermi energy N(E_f) decreases from 5.2 states/formula at 25 GPa to 4.1 states/formula at 50 GPa, which agrees with the slow decreasing of T_c from 28.3 to 53.5 GPa.

To confirm the emergence of a superconducting state under high pressure, we repeated the measurements with new samples for a second run and proved that all the results were reproducible (Figure S2, Supporting Information). Based on the aforementioned results, we can establish a T_c-P phase diagram for $SrSn_2As_2$ as shown in **Figure** 6. Superconductivity was observed at ≈10.3 GPa with a maximum T_c of 4.63 K at 28.3 GPa for $SrSn_2As_2$. The high-pressure in situ synchrotron XRD and Raman spectroscopy reveal evidence of structural transition ≈28.3 GPa, which is in line with the theoretical predictions that the ambient $R\bar{3}m$ phase transforms to the high-pressure

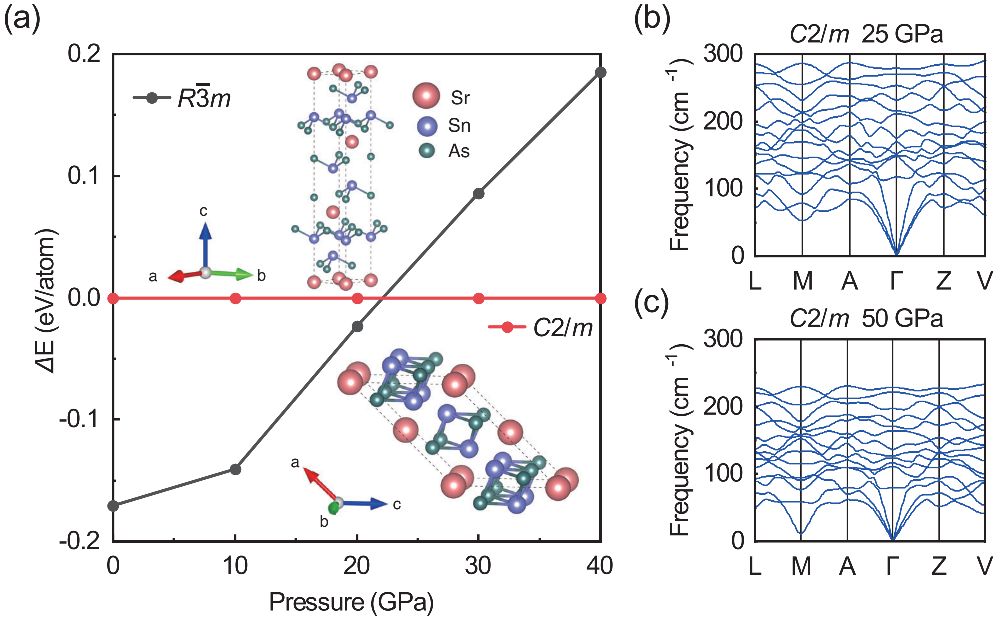

Figure 4. a) The enthalpy difference relative to $R\bar{3}m$ structure at 40 GPa. The calculated phonon spectrum of the predicted $C2/m$ structure at b) 25 GPa and c) 50 GPa.

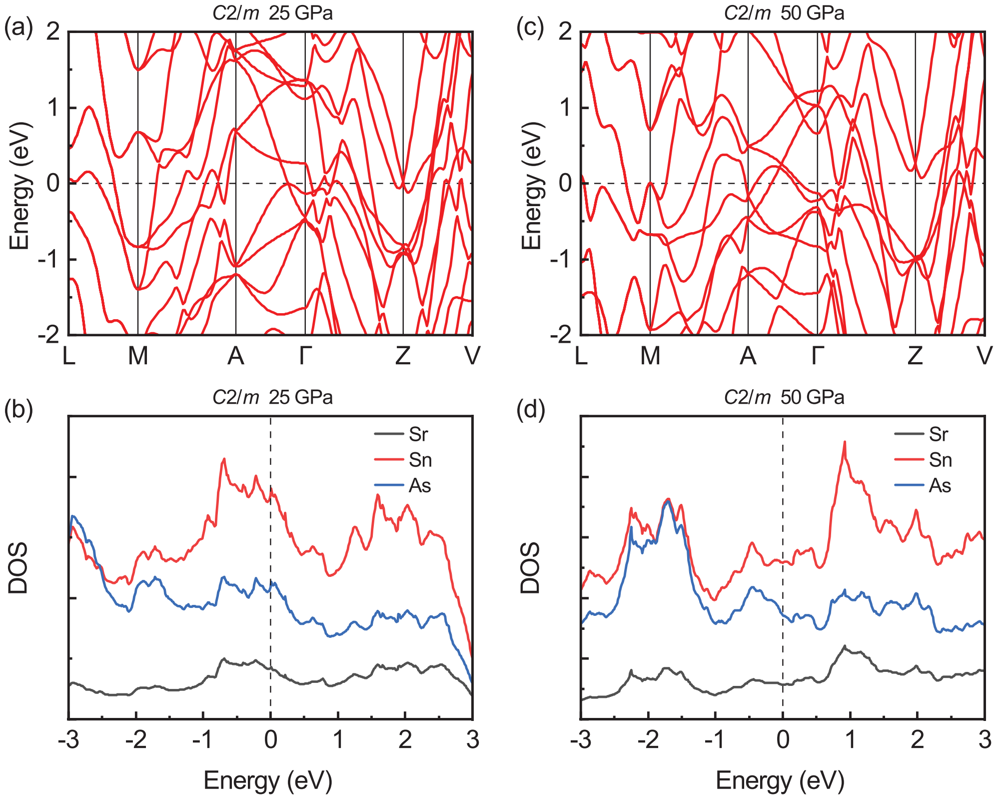

Figure 5. The band structures of the predicted $C2/m$ structure at a) 25 GPa and b) 50 GPa. The corresponding partial density of states (PDOS) at c) 25 GPa and d) 50 GPa. The Fermi energy is set to zero.

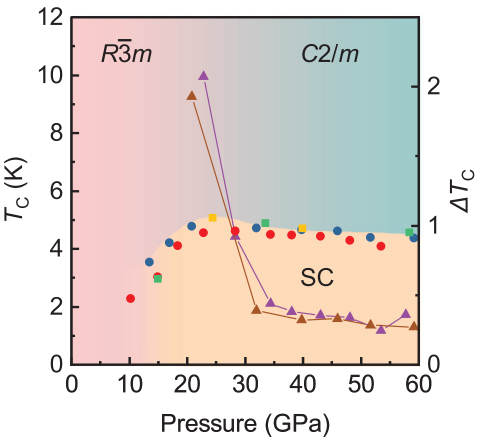

Figure 6. Phase diagram of $SrSn_2As_2$. The left vertical axis represents superconducting transition temperature T_c. Blue, and red solid circles and green, and yellow solid squares represent the T_c in different runs with compression and decompression process, respectively. The right vertical axis represents superconducting transition width ΔT_c. The purple and brown triangular lines represent the superconducting transition width ΔT_c at various pressures. The pink and cyan areas represent two different structures. $SrSn_2As_2$ undergoes a structural transformation from $R\bar{3}m$ to $C/2m$ under high pressure.

$C2/m$ phase. Combining the transition width ΔT_c and theoretical calculations, the T_c-P phase diagram reveals two distinct superconducting regions: SC-I $R\bar{3}m$ phase and SC-II $C2/m$ phase. In the SC-I region, T_c increases with pressure with a broad superconducting transition width. In the SC-I region between 25 and 60 GPa, T_c is monotonically suppressed with external pressure. The suppression of T_c in $SrSn_2As_2$ under pressure can be attributed to a decline in the electronic density of states at the Fermi level.

3. Conclusion

In summary, we have synthesized $SrSn_2As_2$ single crystal and explored the structure and electronic transport properties under high pressure. Our results demonstrate a pressure-induced superconductivity in $SrSn_2As_2$. The pressure-dependent T_c exhibits a nonmonotonic evolution with a maximum value of 4.63 K at 28.3 GPa. Our theoretical calculations, together with high-pressure in situ X-ray diffraction, and Raman spectroscopy measurements, indicate that $SrSn_2As_2$ transforms from the ambient rhombohedral $R\bar{3}m$ phase to the monoclinic $C2/m$ phase above 25 GPa. Our research provides valuable insights into the understanding of the superconductivity in the layered SnAs-based family.

4. Experimental Section

The single crystals of $SrSn_2As_2$ were grown by the self-flux method. In order to obtain high-quality single crystals, pretreatment of starting materials (Sn, Alfa Aesar, 99.999% and As, Alfa Aesar, 99.99%) was performed to remove possible oxide layers on their surface by hydrogen reduction method and sublimation recrystallization method. High-purity starting materials of Sr, Sn, and As were loaded into an Al_2O_3 crucible with the atomic ratio of Sr: Sn: As = 1: 2: 2.2, and sealed into a quartz tube in a vacuum of 8×10^{-4} Pa. The raw materials were reacted and homogenized at 1173 K for several hours, followed by cooling down to 773 K at a rate of 3 K h^{-1}. The crystalline phase of $SrSn_2As_2$ was checked by X-ray diffraction (XRD, Cu $K\alpha$, $\lambda = 1.54184$ Å). The chemical composition of $SrSn_2As_2$ is given by energy-dispersive X-ray spectra (EDX). Electrical transport properties were performed on a physical property measurement system (PPMS, Quantum Design).

Electrical transport measurements under high pressure were performed in a nonmagnetic diamond anvil cell (DAC).[15] A cubic BN/epoxy mixture layer was inserted between the BeCu gasket and electrical leads. Four platinum sheet electrodes were touched to the sample for resistance measurements with the van der Pauw method.[15b,16] Pressure was determined by the ruby luminescence method.[17] High-pressure in situ Raman spectroscopy investigation was performed using a Raman spectrometer (Renishaw in Via, UK) with a laser excitation wavelength of 532 nm and a low-wavenumber filter. Asymmetric DAC with anvil culet sizes of 300 μm was used, with silicon oil as pressure transmitting medium (PTM). High-pressure in situ XRD measurements were performed at beamline BL15U of Shanghai Synchrotron Radiation Facility (X-ray wavelength $\lambda = 0.6199$ Å). A symmetric DAC with anvil culet sizes of 200 μm and a Re gasket were used. Silicon oil was used as the PTM. The 2D diffraction images were analyzed using the FIT2D software.[18] Rietveld refinements of crystal structure under various pressures were performed using the GSAS and the graphical user interface EXPGUI.[19]

We used the machine learning graph theory accelerated crystal structure search method (Magus) to explore the structures of $SrSn_2As_2$ under 30 and 50 GPa.[20] We performed the geometry optimization using the Vienna Ab initio Simulation Package (VASP) based on the density functional theory.[21] The exchange-correlation function was treated by the generalized gradient approximation of Perdew, Burkey, and Ernzerhof.[22] The calculations used a projector-augmented wave (PAW) approach to describe the core electrons and their effects on valence orbitals.[23] The plane-wave kinetic-energy cutoff was set to 600 eV, and the Brillouin zone was sampled by the Monkhorst-Pack scheme of $2\pi \times 0.03$ Å^{-1}. The convergence tolerance was 10^{-6} eV for total energy and 0.003 eV Å^{-1} for all forces. The electronic structure calculations used a denser k-mesh grid of $2\pi \times 0.02$ Å^{-1}. The phonon spectrum was calculated by the PHONOPY program package using the finite displacement method with the supercell $2 \times 2 \times 2$.[24]

Supporting Information

Supporting Information is available from the Wiley Online Library or from the author.

Acknowledgements

W.C., J.W., and Y.L. contributed equally to this work. This work was supported bythe National Natural Science Foundation of China (Grant No. 52272265), the National Key R&D Program of China (Grant Nos. 2018YFA0704300, 2023YFA1607400), and Shanghai Science and Technology Plan (Grant No. 21DZ2260400). Z.W.W. thanks the support from the National Key R&D Program of China (Grant Nos. 2020YFA0308800 and 2022YFA1403400), the Natural Science Foundation of China (Grant No. 92065109), the Beijing Natural Science Foundation (Grant Nos. Z210006 and Z190006). The authors thank the Analytical Instrumentation Center (# SPST-AIC10112914), SPST, ShanghaiTech University, and the Analysis and Testing Center at Beijing Institute of Technology for assistance in facility support. The authors thank the staff from BL15U1 at Shanghai Synchrotron Radiation Facility for assistance during data collection.

Conflict of Interest

The authors declare no conflict of interest.

Data Availability Statement

The data that support the findings of this study are available from the corresponding author upon reasonable request.

Keywords

high-pressure, structure phase transition, superconductivity, Zintl materials

Received: December 10, 2023
Revised: December 27, 2023
Published online:

---

[1] E. Zintl, *Angew. Chem., Int. Ed.* **1939**, *52*, 1.

[2] a) J. D. Corbett, *Angew. Chem., Int. Ed.* **2000**, *39*, 670; b) C. Belin, R. G. Ling, *J. Solid State Chem.* **1983**, *48*, 40.

[3] a) P. Alemany, M. Llunell, E. Canadell, *J. Comput. Chem.* **2008**, *29*, 2144; b) C. Zheng, R. Hoffmann, R. Nesper, H. G. Von Schnering, *J. Am. Chem. Soc.* **1986**, *108*, 1876; c) E. S. Toberer, A. Zevalkink, N. Crisosto, G. J. Snyder, *Adv. Funct. Mater.* **2010**, *20*, 4375; d) P. Rosa, Y. Xu, M. Rahn, J. Souza, S. Kushwaha, L. Veiga, A. Bombardi, S. Thomas, M. Janoschek, E. Bauer, M. Chan, Z. Wang, J. Thompson, N. Harrison, P. Pagliuso, A. Bernevig, F. Ronning, *npj Quantum Mater.* **2020**, *5*, 52; e) Y. Tang, Z. M. Gibbs, L. A. Agapito, G. Li, H.-S. Kim, M. B. Nardelli, S. Curtarolo, G. J. Snyder, *Nat. Mater.* **2015**, *14*, 1223; f) C. Pei, T. Ying, Q. Zhang, X. Wu, T. Yu, Y. Zhao, L. Gao, C. Li, W. Cao, Q. Zhang, A. P. Schnyder, L. Gu, X. Chen, H. Hosono, Y. Qi, *J. Am. Chem. Soc.* **2022**, *144*, 6208; g) G. J. Snyder, M. Christensen, E. Nishibori, T. Caillat, B.o B. Iversen, *Nat. Mater.* **2004**, *3*, 458; h) J.-S. Rhyee, K. H. Lee, S. M. Lee, E. Cho, S. I. Kim, E. Lee, Y. S. Kwon, J. H. Shim, G. Kotliar, *Nature* **2009**, *459*, 965; i) Y. Qi, Z. Gao, L. Wang, D. Wang, X. Zhang, Y. Ma, *New J. Phys.* **2008**, *10*, 123003.

[4] a) W. Cao, H. Yang, Y. Li, C. Pei, Q. Wang, Y. Zhao, C. Li, M. Zhang, S. Zhu, J. Wu, *Phys. Rev. B* **2023**, *108*, 224510; b) C. Pei, T. Ying, Y.i Zhao, L. Gao, W. Cao, C. Li, H. Hosono, Y. Qi, *Matter Radiat. Extrem.* **2022**, *7*, 038404; c) J. Wang, T. Ying, J. Deng, C. Pei, T. Yu, X. Chen, Y. Wan, M. Yang, W. Dai, D. Yang, Y. Li, S. Li, S. Iimura, S. Du, H. Hosono, Y. Qi, J.-G. Guo, *Angew. Chem.* **2023**, *135*, e202216086; d) L.-Y. Feng, R. A. B. Villaos, A. B. Maghirang, Z.-Q. Huang, C.-H. Hsu, H. Lin, F.-C. Chuang, *Sci. Rep.* **2022**, *12*, 4582; e) A. M. Goforth, P. Klavins, J. C. Fettinger, S. M. Kauzlarich, *Inorg. Chem.* **2008**, *47*, 11048; f) E. S. Toberer, A. F. May, G. J. Snyder, *Chem. Mater.* **2010**, *22*, 624; g) C. Chen, W. Xue, S. Li, Z. Zhang, X. Li, X. Wang, Y. Liu, J. Sui, X. Liu, F. Cao, Z. Ren, C.-W. Chu, Y. Wang, Q. Zhang, *Proc. Natl. Acad. Sci. U.S.A.* **2019**, *116*, 2831.

[5] a) K. Shinozaki, Y. Goto, K. Hoshi, R. Kiyama, N. Nakamura, A. Miura, C. Moriyoshi, Y. Kuroiwa, H. Usui, Y. Mizuguchi, *ACS Appl. Energy Mater.* **2021**, *4*, 5155; b) K. Lee, D. Kaseman, S. Sen, I. Hung, Z. Gan, B. Gerke, R. Pöttgen, M. Feygenson, J. Neuefeind, O. I. Lebedev, K. Kovnir, *J. Am. Chem. Soc.* **2015**, *137*, 3622; c) Z. Lin, G. Wang, C. Le, H. Zhao, N. Liu, J. Hu, L. Guo, X. Chen, *Phys. Rev. B* **2017**, *95*, 165201; d) A. M. Ochs, P. Gorai, Y. Wang, M. R. Scudder, K. Koster, C. E. Moore, V. Stevanovic, J. P. Heremans, W. Windl, E. S. Toberer, J. E. Goldberger, *Chem. Mater.* **2021**, *33*, 946; e) Y. Goto, A. Miura, C. Moriyoshi, Y. Kuroiwa, T. D. Matsuda, Y. Aoki, Y. Mizuguchi, *Sci. Rep.* **2018**, *8*, 12852; f) E. J. Cheng, J. M. Ni, F. Q. Meng, T. P. Ying, B. L. Pan, Y. Y. Huang, D. C. Peets, Q. H. Zhang, S. Y. Li, *Europhys. Lett.* **2018**, *123*, 47004; g) K. Ishihara, T. Takenaka, Y. Miao, O. Tanaka, Y. Mizukami, H. Usui, K. Kuroki, M. Konczykowski, Y. Goto, Y. Mizuguchi, T. Shibauchi, *Phys. Rev. B* **2018**, *98*, 020503; h) Y. Hao, G. Yosuke, J. Rajveer, M. Akira, M. Chikako, K. Yoshihiro, *Jpn. J. Appl. Phys.* **2019**, *58*, 83001; i) Y. Goto, A. Yamada, T. D. Matsuda, Y. Aoki, Y. Mizuguchi, *J. Phys. Soc. Jpn.* **2017**, *86*, 123701.

[6] M. D. Nielsen, V. Ozolins, J. P. Heremans, *Energy Environ. Sci.* **2013**, *6*, 570.

[7] a) M. Q. Arguilla, N. D. Cultrara, Z. J. Baum, S. Jiang, R. D. Ross, J. E. Goldberger, *Inorg. Chem. Front.* **2017**, *4*, 378; b) H. Li, W. Gao, Z. Chen, W. Chu, Y. Nie, S. Ma, Y. Han, M. Wu, T. Li, Q. Niu, W. Ning, X. Zhu, M. Tian, *Phys. Rev. B* **2021**, *104*, 054435.

[8] a) X. Gui, I. Pletikosic, H. Cao, H.-J. Tien, X. Xu, R. Zhong, G. Wang, T.-R. Chang, S. Jia, T. Valla, W. Xie, R. J. Cava, *ACS Cent. Sci.* **2019**, *5*, 900; b) H.-C. Chen, Z.-F. Lou, Y.-X. Zhou, Q. Chen, B.-J. Xu, S.-J. Chen, J.-H. Du, J.-H. Yang, H.-D. Wang, M.-H. Fang, *Chin. Phys. Lett.* **2020**, *37*, 047201.

[9] H. Li, S.-Y. Gao, S.-F. Duan, Y.-F. Xu, K.-J. Zhu, S.-J. Tian, J.-C. Gao, W.-H. Fan, Z.-C. Rao, J.-R. Huang, *Phys. Rev. X* **2019**, *9*, 041039.

[10] H. Sun, C. Chen, Y. Hou, W. Wang, Y. Gong, M. Huo, L. Li, J. Yu, W. Cai, N. Liu, *Sci. China: Phys., Mech. Astron.* **2021**, *64*, 118211.

[11] a) L. Zhao, C. Yi, C.-T. Wang, Z. Chi, Y. Yin, X. Ma, J. Dai, P. Yang, B. Yue, J. Cheng, F. Hong, J.-T. Wang, Y. Han, Y. Shi, X. Yu, *Phys. Rev. Lett.* **2021**, *126*, 155701; b) L. Zhao, X. Ma, C. Tian, C. Yi, Y. Shi, F. Hong, X. Yu, Y. Han, J.-T. Wang, *Appl. Phys. Lett.* **2022**, *121*, 202201.

[12] Q. D. Gibson, L. M. Schoop, L. Muechler, L. S. Xie, M. Hirschberger, N. P. Ong, R. Car, R. J. Cava, *Phys. Rev. B* **2015**, *91*, 205128.

[13] L.-Y. Rong, J.-Z. Ma, S.-M. Nie, Z.-P. Lin, Z.-L. Li, B.-B. Fu, L.-Y. Kong, X.-Z. Zhang, Y.-B. Huang, H.-M. Weng, T. Qian, H. Ding, R.-Z. Tai, *Sci. Rep.* **2017**, *7*, 6133.

[14] E. F. Talantsev, K. Stolze, *Supercond. Sci. Technol.* **2021**, *34*, 064001.

[15] a) W. Cao, N. Zhao, C. Pei, Q.i Wang, Q. Zhang, T. Ying, Y. Zhao, L. Gao, C. Li, N. Yu, L. Gu, Y. Chen, K. Liu, Y. Qi, *Phys. Rev. B* **2022**, *105*, 174502; b) C. Pei, J. Zhang, Q. Wang, Y. Zhao, L. Gao, C. Gong, S. Tian, R. Luo, M. Li, W. Yang, Z.-Y. Lu, H. Lei, K. Liu, Y. Qi, *National Science Review* **2023**, *10* nwad034; c) Q. Wang, P. Kong, W. Shi, C. Pei, C. Wen, L. Gao, Y. Zhao, Q. Yin, Y. Wu, G. Li, H. Lei, J. Li, Y. Chen, S. Yan, Y. Qi, *Adv. Mater.* **2021**, *33*, 2102813.

[16] a) C. Pei, J. Zhang, C. Gong, Q. Wang, L. Gao, Y. Zhao, S. Tian, W. Cao, C. Li, Z.-Y. Lu, *Sci. China: Phys., Mech. Astron.* **2022**, *65*, 287412; b) W. Cao, Y. Su, Q. Wang, C. Pei, L. Gao, Y. Zhao, C. Li, N. Yu, J. Wang, Z. Liu, Y. Chen, G. Li, J. Li, Y. Qi, *Chin. Phys. Lett.* **2022**, *39*, 047501.

[17] H. K. Mao, J. Xu, P. M. Bell, *J. Geophys. Res. Solid Earth* **1986**, *91*, 4673.

[18] A. P. Hammersley, S. O. Svensson, M. Hanfland, A. N. Fitch, D. Hausermann, *Int. J. High Press. Res.* **1996**, *14*, 235.

[19] a) A. C. Larson, R. B. Von Dreele, Los Alamos National Laboratory, Los Alamos, New Mexico **2004**; b) B. H. Toby, *J. Appl. Crystallogr.* **2001**, *34*, 210.

[20] a) K. Xia, H. Gao, C. Liu, J. Yuan, J. Sun, H.-T. Wang, D. Xing, *Sci. Bull.* **2018**, *63*, 817; b) H. Gao, J. Wang, Y.u Han, J. Sun, *Fundament. Res.* **2021**, *1*, 466.

[21] a) G. Kresse, J. Furthmüller, *Phys. Rev. B* **1996**, *54*, 11169; b) H. J. Monkhorst, J. D. Pack, *Phys. Rev. B* **1976**, *13*, 5188.

[22] J. P. Perdew, K. Burke, M. Ernzerhof, *Phys. Rev. Lett.* **1996**, *77*, 3865.

[23] P. E. Blöchl, *Phys. Rev. B* **1994**, *50*, 17953.

[24] A. Togo, I. Tanaka, *Scr. Mater.* **2015**, *108*, 1.